



Electron Nuclear Double Resonance of the Chlorophyll Triplet State in the Water-Soluble Chlorophyll Protein from *Brassica oleracea*: Investigation of the Effect of the Binding Site on the Hyperfine Couplings

Alessandro Agostini^{1,2} · Daniel M. Palm² · Harald Paulsen² ·
Marilena Di Valentin¹ · Donatella Carbonera¹

Received: 10 July 2020 / Revised: 3 August 2020
© The Author(s) 2020

Abstract

An investigation of the photoexcited triplet state of chlorophyll (Chl) *a* in the water-soluble chlorophyll protein (WSCP) of *Brassica oleracea* has been carried out by means of electron-nuclear double resonance (ENDOR), achieving a complete assignment of the observed hyperfine couplings corresponding to methine protons and methyl groups of Chl *a* triplet state. The triplet-state properties, and in particular the hyperfine couplings, were found to be similar to those previously reported for Chl *a* in the WSCP of *Lepidium virginicum*. Therefore, the porphyrin ring deformation observed in *Brassica oleracea* WSCP seems to only slightly affect the spin density of ³Chl *a*. This may be relevant when considering the robustness of triplet–triplet energy transfer mechanisms, relying on wavefunction overlap, in systems, such as the photosynthetic light-harvesting complexes, in which Chl triplet states with distorted geometries are involved.

1 Introduction

The water-soluble chlorophyll protein (WSCP) [1] has emerged in recent years as a promising model system for the investigation of tetrapyrroles in a protein environment [2], by virtue of its structural simplicity [3–5], high stability [6–8], and capability to be reconstituted *in vitro* with different tetrapyrroles [9–11]. Upon

✉ Alessandro Agostini
alessandro.agostini.1@unipd.it

✉ Donatella Carbonera
donatella.carbonera@unipd.it

¹ Department of Chemical Sciences, University of Padova, Via Marzolo 1, 35131 Padua, Italy

² Institute of Molecular Physiology, Johannes Gutenberg-University, Johannes-von-Müller-Weg 6, 55128 Mainz, Germany

tetramerization of four identical protein monomers, each binding one tetrapyrrole, a homotetrameric complex in which the tetrapyrroles are organized into a “dimer of dimers” configuration is obtained (Fig. 1A) [3–6]. The four symmetry-related chlorophyll (Chl) binding sites are identical, and therefore, the four bound chromophores experience identical protein surroundings and are spectroscopically equivalent, contrarily to chlorophyll (Chl)-binding complexes involved in photosynthesis, in which tens to hundreds of chromophores are bound in finely tuned individual binding sites [12], resulting in highly complex spectra. It follows that WSCP is an ideal model system for detailed spectroscopic investigation focused on understanding Chl–protein and Chl–Chl interactions [5, 13–20].

Brassicaceae WSCPs are categorized into two subclasses, IIa and IIb, according to their different Chl *alb* ratio [21, 22]. Key amino acids in the protein sequence of class IIa and IIb WSPCs have been linked to their different Chl *alb*

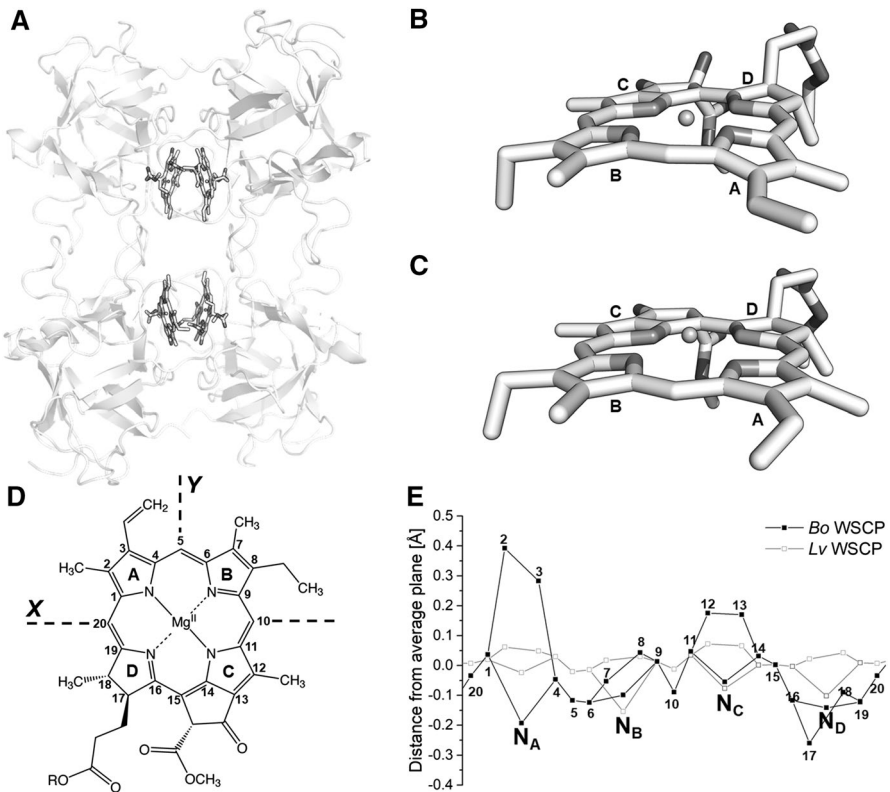


Fig. 1 (A) Structure of the tetrameric WSCP complex from *Brassica oleracea* (PDB ID: 5HPZ [4]). Comparison of the conformations of Chl *a* in *Bo* WSCP (B) [4] and *Lv* WSCP (C) [3]. Phytol chains have been omitted for clarity. (D) Scheme of Chl *a* structure with the orientation of the ZFS axes (the *Z* axis is perpendicular to the molecular plane). The IUPAC numbering scheme has been adopted in the labeling of the Chl *a* structure (R = phytol chain). (E) Plot of the displacement of each tetrapyrrole atom from the plane defined averaging the position of the 24 atoms composing the tetrapyrrolic system for the Chls *a* in *Bo* WSCP [4] and *Lv* WSCP [3] (in black and gray, respectively). The *x*-axis is not in scale

selectivity [10, 19] and to the observed differences in the optical properties of the bound Chls [4, 18, 19, 23]. In particular, the absorption of the Q_y ($S_0 \rightarrow S_1$) band of Chl *a* in class IIa WSCP from *Brassica oleracea* var. *botrytis* (from here on referred to as *Bo*) is 10 nm red-shifted when compared to class IIb WSCP from *Lepidium virginicum* (*Lv*). This shift has been attributed to a combination of electrostatic interactions between the Chl and its protein surrounding and the out-of-plan distortion of the chlorin macrocycle, induced by the steric hindrance exerted by the protein surrounding, in *Bo* WSCP (compare rings A in the Chl *a* structures in Fig. 1b, c, e) [4, 23].

The alterations of the optical properties, originated from the effects of the binding site, may affect the triplet-state properties as well. The role of the Chl triplet state (^3Chl) in oxygen photosensitization, and the importance of the triplet-state wavefunction overlap in photoprotective mechanisms based on triplet–triplet energy transfer [24–27], call for a determination of the effects of the binding sites to the electronic structure of the triplet state in a model system such as WSCP.

Optically detected magnetic resonance (ODMR) and time-resolved electron paramagnetic resonance (TR-EPR) are powerful techniques for the investigation of photoexcited triplet states, and extensive studies employing both these spectroscopies have been performed on Chl-binding proteins [28–30]. Key data are the zero-field splitting (ZFS) parameters *D* and *E*, which are sensitive indicators of the spatial extension and symmetry of the two singly occupied molecular orbitals of the triplet state, and the electron spin polarization that derives from the selective population of the triplet spin sublevels and for this reason is a fingerprint of the mechanism of formation of the triplet state. The ZFS parameters are integral properties of the triplet wavefunction and depend on its overall spatial distribution.

More specific information about the electron distribution in the frontier orbitals is obtained from the electron-nuclear hyperfine coupling (hfc) tensors, from which the distribution of the unpaired electrons of the triplet state is derived. To verify if the $^3\text{Chl } a$ in *Bo* WSCP is affected by the tuning properties of the protein-binding sites, a mapping of the spin density over the molecular structure, with a particular focus onto the portions of the molecules more affected by the Chl deformations, has been carried out in this study. To this purpose, pulse electron-nuclear double resonance (ENDOR), combined with laser excitation, is the best-suited technique [31]. In the case of photo-induced triplet states, due to the large anisotropy of the triplet-state ZFS tensor, this is achieved by performing orientation-selective ENDOR, providing the hfc tensor components of the α and β protons interacting with the triplet electron spins. The technique has been extensively employed to characterize the triplet states of chlorophylls [11, 32–34].

We recently showed that WSCP is suitable for obtaining intense and particularly narrow ENDOR lines of $^3\text{Chl } a$ [11, 32], compared to those obtained in frozen solvents or in other Chl-binding proteins [34], probably by virtue of a high rigidity of the Chl-binding sites in WSCP [11]. Moreover, WSCPs are characterized by a unique photoprotection mechanism that grants a remarkable photostability to the bound Chls [7, 11] even though the ^3Chl state is populated with high yield [11] and it is accessible to oxygen [11, 35], making this complex suitable for extended data collection sessions.

In this work, the first full experimental characterization of *Bo* WSCP $^3\text{Chl } a$ by means of Davies and Mims ENDOR, time-resolved EPR (TR-EPR), and Absorption Detected Magnetic Resonance (ADMR) was carried out. This full characterization is aimed to provide a complete picture of the triplet state, in terms of ZFS parameters, spin polarization properties, and proton hfcs, including small (< 5 MHz) contributions from the Mims spectra. Thus, a direct comparison between all the magnetic observables of $^3\text{Chl } a$ in two species, i.e., *Brassica oleracea* and *Lepidium virginicum*, having different ring geometries and local protein environment, has been possible.

2 Experimental

2.1 Sample Preparation

Protein overexpression in *E. coli* and subsequent purification have been performed as previously reported [11]. The purified *Brassica oleracea* WSCP apoprotein was reconstituted with Chl *a* as previously described [19].

The samples for the ADMR measurements were diluted with degassed glycerol added to a final concentration of 60% (v/v) to obtain homogeneous and transparent matrices upon freezing. After the glycerol addition, performed immediately before the insertion into the cryostat to avoid sample degradation [36], the final Chl concentration of the samples was 100 $\mu\text{g/mL}$. In all measurements, the temperature was 1.8 K.

WSCP was concentrated up to a Chl *a* concentration of 700 $\mu\text{g/mL}$ for TR-EPR and ENDOR measurements. Oxygen was removed by flushing nitrogen in the sample tube before freezing. Residual oxygen was removed adding the glucose/glucose oxidase/catalase system [37]. Glycerol, previously degassed by several cycles of freezing and pumping, was added (60% v/v) just before freezing to obtain a transparent matrix.

2.2 ADMR Experiments

ADMR spectra were acquired in a home-built set-up which has been previously described in detail [20]. Namely, a 250 W halogen lamp (Philips) was employed as a light source, filtered through a 10 cm water filter, and focused on the sample cell immersed in a helium bath cryostat. The sample absorbance was detected with a standard straight geometry through a monochromator (Jobin Yvon, mod.HR250) by a Si-photodiode (OSI-Centronix). The microwave resonator, where the sample cell is inserted, consists of a slow pitch helix. The microwaves produced by an HP8559b sweep oscillator equipped with an HP83522s plug-in and amplified by a TWT Sco-Nuclétudes mod 10-46-30 amplifier were on/off amplitude modulated for selective amplification, and the signal from the detector was demodulated and amplified using a Lock-In amplifier (EG&G, mod 5210). The analog output is connected to a computer-controlled analog-to-digital converter.

2.3 TR-EPR Experiments

X-band TR-EPR experiments were performed on a modified Bruker ER200D spectrometer with an extended detection bandwidth (6 MHz), allowing a response time of about 700 ns. Laser excitation at 532 nm (5 mJ per pulse and repetition rate of 50 Hz) was provided by the second harmonic of an Nd:YAG laser (Quantel Brilliant) in a high-Q cylindrical TE_{011} resonant cavity, microwave frequency: 9.39 GHz. The experiments were carried out with a microwave power in the cavity of 2 mW. The temperature was controlled with a nitrogen flow cryostat. The signal was recorded with a LeCroy LT344 digital oscilloscope, triggered by the laser pulse. The spectra were recorded averaging 800 transient signals at each field position. To eliminate the laser background signal, transients accumulated at off-resonance field positions were subtracted from those on resonance.

Simulations of the powder spin-polarized triplet spectra were performed using a program written in Matlab[®], with the aid of the EasySpin routine (ver. 5.2.25) [38], based on the full diagonalization of the triplet-state spin Hamiltonian, including the Zeeman and electron–electron magnetic dipole interactions, considering a powder distribution of molecular orientations with respect to the magnetic field direction [39]. Input parameters are the triplet-state sublevel populations, the ZFS parameters, the linewidth, and the isotropic g value.

2.4 ENDOR Experiments

X-band pulse ENDOR experiments were performed on a Bruker Elexsys E580 spectrometer. The radiofrequency (RF) amplifier was either AR751-150 W or ENI A-500 W. Pulsed Laser excitation at 532 nm (5 mJ per pulse and repetition rate of 10 Hz) was provided by the second harmonic of an Nd:YAG laser (Quantel Brilliant) in a dielectric ENDOR cavity (EN4118X-MD4), microwave frequency: 9.75 GHz. The temperature was controlled with a Helium cryostat with optical access (Oxford CF935) driven by a temperature controller (Oxford ITC503).

Preliminary Field-swept Electron spin echo (ESE) spectra were recorded using a two-pulse ESE sequence according to the scheme: flash-DAF- $\pi/2$ - τ - π - τ -echo. ESE-detected kinetics at the triplet canonical orientations were recorded using a two-pulse (flash- $\pi/2$ - τ - π - τ -echo) ESE sequence. The $\pi/2$ -pulse was of 16 ns and the delay τ was set at 292 ns.

Davies ENDOR experiments were performed using the microwave pulse sequence (flash- π -T- $\pi/2$ - τ - π - τ -echo) with an inversion π pulse of 200 ns, T of 8 μ s and an RF pulse of 6 μ s. The detection sequence was similar to the field-swept ESE experiment, with τ of 292 ns for Z_1 and 536 ns for X_1 and Y_1 .

Mims ENDOR experiments were recorded using the microwave pulse sequence (flash- $\pi/2$ - τ - $\pi/2$ -T- $\pi/2$ -echo), with 16 ns pulse duration, in conjunction with an RF pulse of 6 μ s duration, starting 0.8 μ s after the second microwave pulse. The delay τ was variable, and the time T was 8 μ s to accommodate the RF pulse. Mims ENDOR spectra were recorded at different τ values (from 240 to 380 ns

for Z_1 and from 456 to 576 ns for X_1 and Y_1) and added together to eliminate τ -dependent blind spots. Pulse ENDOR spectra were accumulated for ≈ 15 h.

3 Results and Discussion

3.1 ADMR Spectra

Continuous illumination at cryogenic temperatures (1.8 K) of Chl *a*-reconstituted *B_o* WSCP leads to the formation of a steady-state population of $^3\text{Chl } a$, which can be detected by ADMR, monitoring the transmittance of the sample at 680 nm, corresponding to the Q_y absorption band, while sweeping the microwave field in a microwave-frequency range characteristic for $^3\text{Chl } a$. The spectra detected at the absorption maximum (680 nm) are reported in Fig. 2. The positions of the $|D|-|E|$ and $|D|+|E|$ transitions (721 and 947 MHz, respectively; note that, as previously reported for $^3\text{Chls}$, the $2|E|$ transition was too weak to be detected) allowed a precise calculation of the values of the ZFS parameters $|D|$ and $|E|$ ($|D|=0.028\text{ cm}^{-1}$ and $|E|=0.0038\text{ cm}^{-1}$), which are close to those previously reported for L_v WSCP ($|D|=0.029\text{ cm}^{-1}$ and $|E|=0.0037\text{ cm}^{-1}$ [20]). The similarity points towards a similar electronic distribution on the single Chl *a* on which the triplet state is localized, as previously reported for L_v WSCP [11]. However, for more detailed information, TR-EPR and ENDOR spectra have been collected.

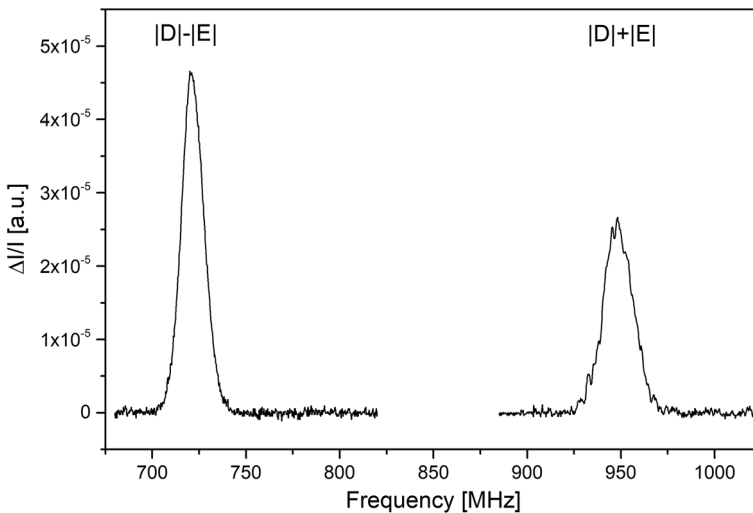


Fig. 2. ^3Chl ADMR spectra of *B_o* WSCP Chls *a*. 680 nm transmitted light was collected through a monochromator (1 nm slits). $T=1.8$ K

3.2 TR-EPR Spectra

Low-temperature TR-EPR spectra of $^3\text{Chl } a$ were measured on *Bo* WSCP (Fig. 3), with a time evolution of the TR-EPR spectra following the common behavior reported for $^3\text{Chls}$ [40, 41]. As expected for a photoexcited triplet state, a symmetric spectrum characterized by both absorptive and emissive transitions has been measured [42, 43]. This spectral feature is originated from the anisotropy of the population of the triplet sublevels, that in the case of a triplet state generated from inter-system crossing (ISC) from the excited singlet state reflects the selective population of the zero-field triplet sublevels starting from the excited singlet state. The population of the high-field triplet sublevels can be obtained starting from those of the zero-field triplet sublevels, for example, for molecules with X parallel to the magnetic field, $p_0 = p_x$ and $p_{\pm 1} = \frac{1}{2}(p_y + p_z)$. Thus, the intensity of the two transitions $m_s = 0$ to $m_s = +1$ (X_{\parallel}) and $m_s = 0$ to $m_s = +1$ (X_{\parallel}) is equal and opposite, a feature shared by all the pairs of transitions corresponding to each orientation of the molecule relative to the magnetic field. This feature originates from the characteristic symmetry of ISC triplet states.

The wide spectrum of a powder or frozen solution sample is the sum of transitions that originate for every orientation of the molecules with respect to the magnetic field. In these spectra, the transitions of molecules with one of the ZFS axes parallel to the magnetic field (namely, canonical orientations) can be easily identified as they are localized at field positions corresponding to turning points in the EPR spectrum (see Fig. 3). The sign (e =emission, a =absorption) of the canonical transitions is commonly used to classify the polarization of triplet states. The initial

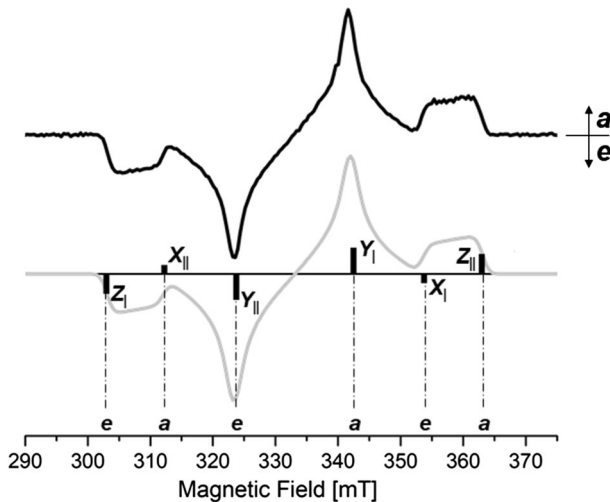


Fig. 3 TR-EPR spectrum of Chl *a* in *Bo* WSCP (upper black line), taken 700 ns after the laser pulse. The spectrum has been collected at 130 K. The simulated triplet spectrum (lower gray line) has been calculated using the following parameters: $D = 0.028 \text{ cm}^{-1}$, $E = -0.0036 \text{ cm}^{-1}$, $(p_y - p_z) : (p_x - p_z) = 1 : 0.267$, and isotropic linewidth $lw = 1.5 \text{ mT}$. The sign and intensity of the $m_s = 0$ to $m_s = +1$ (X_{\parallel} , Y_{\parallel} , and Z_{\parallel}) and $m_s = 0$ to $m_s = -1$ (X_{\perp} , Y_{\perp} , and Z_{\perp}) transitions for the canonical orientations are marked with black bars

polarization pattern of the *Bo* WSCP $^3\text{Chl } a$ spectrum is *eaeaea* like in *Lv* WSCP [11], with only minor changes of the relative population probabilities that have been highlighted by spectral simulation (Fig. 3). Therefore, this polarization pattern, that is more similar to those reported for $^3\text{Chl } a$ in organic solvent (2-methyltetrahydrofuran, MTHF) [44], rather than for $^3\text{Chl } a$ in antenna proteins previously investigated [39, 45–48], seems to be intrinsic to WSCPs and to be almost unaffected by the ring deformation and the minor changes in the Chl-binding sites.

3.3 ENDOR Spectra

The field positions highlighted in the TR-EPR spectrum, corresponding to the canonical triplet orientations, allow the selective excitation of molecules with the ZFS tensor axes (*X*, *Y*, or *Z*) parallel to the magnetic field [49], and the measurement of A_{ii} hfc tensor components of protons in the reference frame of the ZFS tensor. Thus, by collecting the ENDOR spectra at these field positions, the components of the proton hfc tensors along each ZFS direction are obtained, including their sign relative to that of the ZFS parameter *D*.

As an example, we consider the triplet spin energy levels for the *X* orientation, including first-order hyperfine interaction with one proton A_{XX} , for $D > 0$, as expected for a *Chl } a* molecule which is characterized by a discoid shape. For each EPR transition, there are two ENDOR resonance frequencies at:

$$\begin{aligned} \nu_{\text{ENDOR}}(0) &= \nu_{\text{H}} \text{ and } \nu_{\text{ENDOR}}(1) = \nu_{\text{H}} - A_{XX} \text{ if } A_{XX} > 0 \text{ or } \nu_{\text{ENDOR}}(1) \\ &= \nu_{\text{H}} + A_{XX} \text{ if } A_{XX} < 0, \end{aligned}$$

for the $m_s = 0$ to $m_s = +1$ EPR transition (X_{\perp}), and

$$\begin{aligned} \nu_{\text{ENDOR}}(0) &= \nu_{\text{H}} \text{ and } \nu_{\text{ENDOR}}(-1) = \nu_{\text{H}} + A_{XX} \text{ if } A_{XX} > 0 \text{ or } \nu_{\text{ENDOR}}(-1) \\ &= \nu_{\text{H}} - A_{XX} \text{ if } A_{XX} < 0, \end{aligned}$$

for the $m_s = 0$ to $m_s = -1$ EPR transition (X_{\parallel}), where ν_{H} is the proton Larmor frequency.

It follows that the ENDOR transitions are either at the higher or lower frequency side with respect to the central ν_{H} transition, depending on the specific canonical transition. For the X_{\perp} transition, depending on the sign of A_{XX} , the ENDOR lines occur on the low (if $A_{XX} > 0$) or high (if $A_{XX} < 0$) frequency side. An opposite situation is encountered for the X_{\parallel} transition. Therefore, if the sign of the ZFS parameter *D* is known, the sign of the hfcs can be directly derived from the spectral position corresponding to the lines at higher/lower frequencies with respect to ν_{H} . Moreover, it is sufficient to collect the ENDOR spectra at just half of the field positions corresponding to the EPR spectrum turning points, one for each canonical orientation.

The Davis and the Mims ENDOR spectra have been measured at the field positions X_{\perp} , Y_{\perp} , and Z_{\perp} , to have the signals corresponding to negative values of the hfcs in the most sensitive region of the spectrum, i.e., the region at higher frequencies with respect to the free proton transition. This is an experimental choice commonly

adopted in the case of ENDOR [34, 50, 51], aimed to collect spectra in which the intense signals originated from rotating methyl groups, having positive hfcs, are on the low RF side of the spectrum, which is characterized by lower sensitivity. The use of the Mims ENDOR technique is aimed to detect small hfcs with higher sensitivity compared to Davies ENDOR to search for possible differences among the WSCP complexes.

The ENDOR spectra of *Bo* WSCP are well resolved (Fig. 4) and the frequencies of the resolved lines are reported in Table 1 along with the previously determined signals for *Lv* WSCP [11], as well as the benchmark $^3\text{Chl } a$ hfcs calculated by means of a DFT approach [32]. From this comparison, the peaks in the Davies spectra were assigned, similarly to previously determined ENDOR spectra of $^3\text{Chl } a$ [11, 34], to the β protons of methyls 2, 7, and 12 in the negative portion of the spectrum and the α protons of methines 5, 10, and 20 in the positive portion of the spectrum, that are the protons expected to have the strongest hfcs [32]. The ENDOR spectrum corresponding to the X_I transition has poor signal-to-noise ratio due to the low net initial polarization of the EPR signal at this orientation. The spectrum exhibits narrow negative signals, attributable to signals originated from the methyl groups 7 and 12 of molecules with different orientations.

Although the direct comparison of the triplet ENDOR spectra of the $\text{Chl } a$ in *Bo* and *Lv* WSCPs reveals a very similar transition patterns (Table 1), the peaks

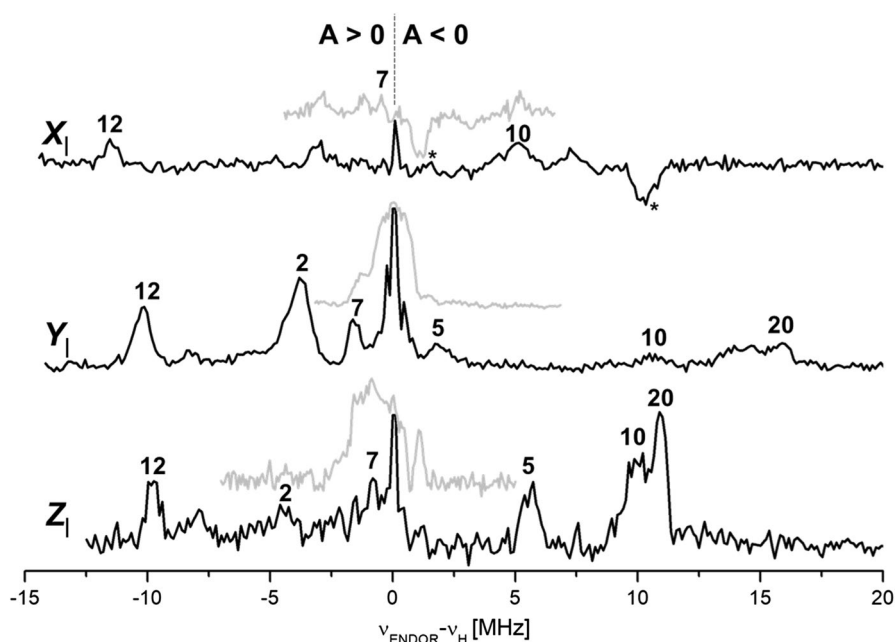


Fig. 4 X-band pulse Davies (black) and Mims (gray) proton ENDOR spectra of *Bo* WSCP $^3\text{Chl } a$, recorded along the X_I , Y_I , and Z_I EPR field positions (366.1 mT, 355.7 mT, and 316.8 mT, respectively). The frequency scale gives the deviation from ν_H . The intense central ν_H lines in the Davies spectra have been cropped for a better comparison. The assignment label refers to Fig. 1D. The experimental details are given in the “Material and methods”

Table 1 Calculated and experimental hfcs of $^3\text{Chl } a$ protons

Hyperfine coupling ^a [MHz]	10 (CH)	20 (CH)	5 (CH)	7 (CH ₃)	12 (CH ₃)	2 (CH ₃)
ENDOR						
<i>Bo</i> WSCP						
A_X	-5.0	n.d	n.d	+0.5	+11.3	n.d
A_Y	-15.0	-10.5	-1.8	+1.6	+10.1	+4.2
A_Z	-10.9	-9.9	-5.7	+0.9	+9.9	+4.4
A_{iso}	-10.3	-	-	+1.0	+10.4	-
<i>Lv</i> WSCP ^b						
A_X	-4.4	-2.3	-10.5	+0.6	+11.6	+5.3
A_Y	-15.6	-12.0	-1.6	+1.7	+10.4	+4.5
A_Z	-10.7	-8.8	-5.0	+0.9	+10.1	+4.3
A_{iso}	-10.2	-7.7	-5.7	+1.1	+10.7	+4.7
DFT^c						
A_X	-2.33	-1.68	-5.52	+1.09	+12.16	+5.66
A_Y	-8.26	-8.08	-1.09	+1.61	+10.87	+4.63
A_Z	-6.42	-6.12	-4.65	+0.64	+10.32	+4.20
A_{iso}	-5.67	-5.30	-3.76	+1.11	+11.12	+4.83

α and β protons are displayed (for β protons, only those with $|A_{\text{iso}}| > 1$ MHz). The *Bo* WSCP experimental values were extracted from the Davies and Mims ENDOR spectra, as shown in Fig. 3, whereas the *Lv* WSCP experimental values and the DFT calculated values are derived from the previous investigations [11, 32]

^aThe X, Y, Z, subscripts of the hf components are referred to the ZFS reference frame

^bPreviously published in [11]

^cThe hfc tensors have been previously calculated in [32], level of theory: COSMO-BP86/QZ4P//BP86/TZ2P

attributed to methines 5 and 20 are affected by the change in the Chl *a*-binding site, with a 10% increase of the coupling in the case of methine 5, and a reduction of the anisotropy of the hfc tensor in the case of methine 20. As these are the two methines flanking the pyrrole ring that in *Bo* WSCP is distorted out of plane from the binding site (ring A [4], see Fig. 1e), a role of this macrocycle deformation in a perturbation of the polarization mechanism responsible for these hfcs can be proposed.

The spin density distribution on the nuclei is closely related to the electronic wavefunction, since it probes the coefficients of the atomic orbitals contributing to the HOMO and LUMO where the two unpaired electrons are localized. The spin density mapping provided by this ENDOR characterization involves various positions of the tetrapyrrole macrocycle, including the pyrrole directly involved in the molecular distortion, even though the local probe provided by the vinyl group is missing. The hfcs of the hydrogens in close vicinity to ring A are the most affected (namely methines 5 and 20), but still the discrepancy is of about 10%. Surprisingly, the methyl in position 2 is largely unaffected by out of plane deformation of the pyrrole to which is bound. In conclusion, the results point towards a small redistribution

of the triplet-state spin density following a macrocycle deformation of the magnitude generated by the *Bo* WSCP-binding sites. Additionally, also the other spectroscopic observables such as ZFS parameters and spin populations, were found to be affected only marginally. In principle, a structural rearrangement of the tetrapyrrole ring in the triplet state cannot be excluded [26], but given the steric crowdedness of the binding site and the interaction of specific amino acids with the out of plane pyrrole [4, 19], we expect the deformation observed in the structure of the Chl [4] to be retained in the triplet state, as well.

This observed low sensitivity to macrocycle deformation is an important trait of $^3\text{Chl } a$, as both its photosensitization of molecular oxygen to highly oxidizing singlet state and its quenching by carotenoids via triplet–triplet energy transfer in light-harvesting complexes require orbital overlap of the two interacting molecules [24–27, 52]. This last point, in particular, may be relevant, since Chls are known to be bound in photosynthetic proteins with variable degrees of ring deformation, as this is one of the molecular strategies adopted by Chl-binding proteins to tune their energy [53–55]. Thus, the observed weak dependence of the triplet-state wavefunction on the different binding sites, as observed in class IIa and IIb WSCPs, is expected to concur to the robustness of the natural photoprotective mechanisms, since different binding sites and naturally occurring fluctuations of the Chls surroundings leading to ring deformations are expected not to cause major modifications in the electronic couplings determining the triplet–triplet energy transfer efficiency.

4 Conclusions

In this investigation, based on ADMR, TR-EPR, and ENDOR spectroscopies, an accurate picture of the triplet-state electronic structure was provided. The hyperfine measurements of the $^3\text{Chl } a$ in *Bo* WSCP pointed out that the triplet-state wavefunction distribution onto the Chl *a* structure is only slightly affected by the macrocycle deformation and the change in electrostatic interactions with the surrounding, which instead were proven to significantly affect the singlet state wavefunction.

Funding Financial support from the University of Padova to A.A. and D.C. (P-DiSC-2019) and to M.D.V. (PRAT2014–CPDA145097/14) is gratefully acknowledged. Open access funding provided by Università degli Studi di Padova within the CRUI-CARE Agreement.

Data and Materials All data needed to evaluate the conclusions in the paper are present in the paper.

Compliance with Ethical Standards

Conflict of interest The authors declare no competing interests.

Open Access This article is licensed under a Creative Commons Attribution 4.0 International License, which permits use, sharing, adaptation, distribution and reproduction in any medium or format, as long as you give appropriate credit to the original author(s) and the source, provide a link to the Creative Commons licence, and indicate if changes were made. The images or other third party material in this article are included in the article's Creative Commons licence, unless indicated otherwise in a credit line to the

material. If material is not included in the article's Creative Commons licence and your intended use is not permitted by statutory regulation or exceeds the permitted use, you will need to obtain permission directly from the copyright holder. To view a copy of this licence, visit <http://creativecommons.org/licenses/by/4.0/>.

References

1. T. Murata, N. Murata, *Carnegie Inst. Wash. Yearb.* **70**, 504–507 (1971)
2. G. Renger, J. Pieper, C. Theiss, I. Trostmann, H. Paulsen, T. Renger, H.J. Eichler, F.-J. Schmitt, *J. Plant Physiol.* **168**, 1462–1472 (2011)
3. D. Horigome, H. Satoh, N. Itoh, K. Mitsunaga, I. Oonishi, A. Nakagawa, A. Uchida, *J. Biol. Chem.* **282**, 6525–6531 (2007)
4. D. Bednarczyk, O. Dym, V. Prabahar, Y. Peleg, D.H. Pike, D. Noy, *Angew. Chemie Int. Ed.* **55**, 1–6 (2016)
5. A. Agostini, E. Meneghin, L. Gewehr, D. Pedron, D.M. Palm, D. Carbonera, H. Paulsen, E. Jaenicke, E. Collini, *Sci. Rep.* **9**, 18255 (2019)
6. D.M. Palm, A. Agostini, S. Tenzer, B.M. Gloeckle, M. Werwie, D. Carbonera, H. Paulsen, *Biochemistry* **56**, 1726–1736 (2017)
7. D.M. Palm, A. Agostini, A.-C. Pohland, M. Werwie, E. Jaenicke, H. Paulsen, *ACS Omega* **4**, 7971–7979 (2019)
8. S. Takahashi, A. Uchida, K. Nakayama, H. Satoh, *Protein J.* **33**, 75–84 (2014)
9. K. Schmidt, C. Fufezan, A. Krieger-Liszky, H. Satoh, H. Paulsen, *Biochemistry* **42**, 7427–7433 (2003)
10. P. Girr, J. Kilper, A.-C. Pohland, H. Paulsen, *Photochem. Photobiol. Sci.* **19**, 695–712 (2020).
11. A. Agostini, D.M. Palm, F.-J. Schmitt, M. Albertini, M. Di Valentin, H. Paulsen, D. Carbonera, *Sci. Rep.* **7**, 7504 (2017)
12. R. Croce, *New Phytol.* (2020). <https://doi.org/10.1111/nph.16758>
13. T. Renger, M.E. Madjet, F. Müh, I. Trostmann, F.-J. Schmitt, C. Theiss, H. Paulsen, H.J. Eichler, A. Knorr, G. Renger, *J. Phys. Chem. B.* **113**, 9948–9957 (2009)
14. J. Pieper, M. Rätsep, I. Trostmann, H. Paulsen, G. Renger, A. Freiberg, *J. Phys. Chem. B.* **115**, 4053–4065 (2011)
15. J. Pieper, M. Rätsep, I. Trostmann, H. Paulsen, G. Renger, A. Freiberg, *J. Phys. Chem. B.* **115**, 4042–4052 (2011)
16. J. Alster, H. Lokstein, J. Dostál, A. Uchida, D. Zigmantas, *J. Phys. Chem. B.* **118**, 3524–3531 (2014)
17. A. Kell, D. Bednarczyk, K. Acharya, J. Chen, D. Noy, R. Jankowiak, *Photochem. Photobiol.* **92**, 428–435 (2016)
18. E. Fresch, E. Meneghin, A. Agostini, H. Paulsen, D. Carbonera, E. Collini, *J. Phys. Chem. Lett.* **11**, 1059–1067 (2020)
19. D.M. Palm, A. Agostini, V. Aversch, P. Girr, M. Werwie, S. Takahashi, H. Satoh, E. Jaenicke, H. Paulsen, *Nat. Plants.* **4**, 920–929 (2018)
20. A. Agostini, D.M. Palm, H. Paulsen, D. Carbonera, *J. Phys. Chem. B.* **122**, 6156–6163 (2018)
21. H. Satoh, A. Uchida, K. Nakayama, M. Okada, *Plant Cell Physiol.* **42**, 906–911 (2001)
22. V. Prabahar, L. Afriat-Jurnou, I. Paluy, Y. Peleg, D. Noy, *FEBS J.* **287**, 991–1004 (2019)
23. Y. Lahav, D. Noy, I. Schapiro, *ChemRxiv* (2020). Preprint. <https://doi.org/10.26434/chemrxiv.12380027.v1>
24. M. Di Valentin, C.E. Tait, E. Salvadori, L. Orian, A. Polimeno, D. Carbonera, *Biochim. Biophys. Acta Bioenerg.* **2014**, 85–97 (1837)
25. M. Di Valentin, D. Carbonera, *J. Phys. B At. Mol. Opt. Phys.* **50**, 162001 (2017)
26. J. Ho, E. Kish, D.D. Méndez-Hernández, K. WongCarter, S. Pillai, G. Kodis, J. Niklas, O.G. Poluektov, D. Gust, T.A. Moore, A.L. Moore, V.S. Batista, B. Robert, *Proc. Natl. Acad. Sci. USA* **114**, E5513–E5521 (2017)
27. G.L. Closs, P. Piotrowiak, J.M. MacInnis, G.R. Fleming, *J. Am. Chem. Soc.* **110**, 2652–2653 (1988)
28. D.E. Budil, M.C. Thurnauer, *Biochim. Biophys. Acta Bioenerg.* **1057**, 1–41 (1991)
29. D. Carbonera, *Photosynth. Res.* **102**, 403–414 (2009)

30. R.H. Clarke, *Triplet State ODMR Spectroscopy: Techniques and Applications to Biophysical Systems* (Wiley, New York, 1982)
31. L. Kulik, W. Lubitz, *Photosynth. Res.* **102**, 391–401 (2009)
32. A. Agostini, M.G. Dal Farra, H. Paulsen, A. Polimeno, L. Orian, M. Di Valentin, D. Carbonera, *J. Phys. Chem. B.* **123**, 8232–8239 (2019)
33. M. Di Valentin, C. Kay, G. Giacometti, K. Mobius, *Chem. Phys. Lett.* **248**, 434–441 (1996)
34. F. Lendzian, R. Bittl, A. Telfer, W. Lubitz, *Biochim. Biophys. Acta Bioenerg.* **1605**, 35–46 (2003)
35. A. Agostini, D.M. Palm, H. Paulsen, D. Carbonera, *J. Phys. Chem. Lett.* **9**, 672–676 (2018)
36. D. Carbonera, P. Collareta, G. Giacometti, *Biochim. Biophys. Acta Bioenerg.* **1322**, 115–128 (1997)
37. I. Yruela, P.J.M. van Kan, M.G. Müller, A.R. Holzwarth, *FEBS Lett.* **339**, 25–30 (1994)
38. S. Stoll, A. Schweiger, *J. Magn. Reson.* **178**, 42–55 (2006)
39. M. Di Valentin, S. Ceola, E. Salvadori, G. Agostini, D. Carbonera, *Biochim. Biophys. Acta Bioenerg.* **1777**, 186–195 (2008)
40. D. Carbonera, M. Di Valentin, G. Agostini, G. Giacometti, P.A. Liddell, D. Gust, A.L. Moore, T.A. Moore, *Appl. Magn. Reson.* **13**, 487–504 (1997)
41. O. Gonen, H. Levanon, *J. Phys. Chem.* **88**, 4223–4228 (1984)
42. S. Richert, C.E. Tait, C.R. Timmel, *J. Magn. Reson.* **280**, 103–116 (2017)
43. Y. Hou, X. Zhang, K. Chen, D. Liu, Z. Wang, Q. Liu, J. Zhao, A. Barbon, *J. Mater. Chem. C.* **7**, 12048–12074 (2019)
44. M. Di Valentin, S. Ceola, G. Agostini, A. Telfer, J. Barber, F. Böhles, S. Santabarbara, D. Carbonera, *Mol. Phys.* **105**, 2109–2117 (2007)
45. M. Di Valentin, E. Meneghin, L. Orian, A. Polimeno, C. Büchel, E. Salvadori, C.W.M. Kay, D. Carbonera, *Biochim. Biophys. Acta Bioenerg.* **2013**, 1226–1234 (1827)
46. D. Carbonera, A. Agostini, M. Di Valentin, C. Gerotto, S. Basso, G.M. Giacometti, T. Morosinotto, *Biochim. Biophys. Acta Bioenerg.* **2014**, 1235–1246 (1837)
47. M. Di Valentin, F. Biasibetti, S. Ceola, D. Carbonera, *J. Phys. Chem. B.* **113**, 13071–13078 (2009)
48. M. Di Valentin, E. Salvadori, G. Agostini, F. Biasibetti, S. Ceola, R. Hiller, G.M. Giacometti, D. Carbonera, *Biochim. Biophys. Acta - Bioenerg.* **1797**, 1759–1767 (2010)
49. F.J.E. van Mieghem, K. Satoh, A.W. Rutherford, *Biochim. Biophys. Acta Bioenerg.* **1058**, 379–385 (1991)
50. J. Niklas, T. Schulte, S. Prakash, M. van Gestel, E. Hofmann, W. Lubitz, *J. Am. Chem. Soc.* **129**, 15442–15443 (2007)
51. M. Di Valentin, S. Ceola, E. Salvadori, G. Agostini, G.M. Giacometti, D. Carbonera, *Biochim. Biophys. Acta Bioenerg.* **1777**, 1355–1363 (2008)
52. A.A. Krasnovskii Jr., *Biofizika* **39**, 236–250 (1994)
53. G. Zucchelli, D. Brogioli, A.P. Casazza, F.M. Garlaschi, R.C. Jennings, *Biophys. J.* **93**, 2240–2254 (2007)
54. G. Zucchelli, S. Santabarbara, R.C. Jennings, *Biochemistry* **51**, 2717–2736 (2012)
55. K. Saito, Y. Umena, K. Kawakami, J. Shen, N. Kamiya, H. Ishikita, *Biochemistry* **51**, 4290–4299 (2012)